



Title	A study of FeNx/C catalysts for the selective oxidation of unsaturated alcohols by molecular oxygen
Author(s)	Zhang, Jinping; Nagamatsu, Shinichi; Du, Junmou; Tong, Chaoli; Fang, Huihuang; Deng, Dehui; Liu, Xi; Asakura, Kiyotaka; Yuan, Youzhu
Citation	Journal of catalysis, 367, 16-26 <a href="https://doi.org/10.1016/j.jcat.2018.08.004">https://doi.org/10.1016/j.jcat.2018.08.004</a>
Issue Date	2018-11
Doc URL	<a href="http://hdl.handle.net/2115/79699">http://hdl.handle.net/2115/79699</a>
Rights	© 2018. This manuscript version is made available under the CC-BY-NC-ND 4.0 license <a href="https://creativecommons.org/licenses/by-nc-nd/4.0/">https://creativecommons.org/licenses/by-nc-nd/4.0/</a>
Rights(URL)	<a href="https://creativecommons.org/licenses/by-nc-nd/4.0/">https://creativecommons.org/licenses/by-nc-nd/4.0/</a>
Type	article (author version)
File Information	AsakuraYuanJCAT.pdf



[Instructions for use](#)

# **A Study of FeN<sub>x</sub>/C Catalyst for the Selective Oxidation of Unsaturated Alcohols by Molecular Oxygen**

*Jinping Zhang<sup>1</sup>, Shinichi Nagamatsu<sup>2</sup>, Junmou Du<sup>1</sup>, Chaoli Tong<sup>1</sup>, Huihuang Fang<sup>1</sup>, Dehui Deng<sup>1,3</sup>, Xi Liu<sup>4</sup>, Kiyotaka Asakura<sup>2\*</sup>, and Youzhu Yuan<sup>1\*</sup>*

<sup>1</sup> State Key Laboratory of Physical Chemistry of Solid Surfaces, National Engineering Laboratory for Green Chemical Productions of Alcohols-Ethers-Esters, *iChEM*, College of Chemistry and Chemical Engineering, Xiamen University, Xiamen 361005, China

<sup>2</sup> Institute for Catalysis, Hokkaido University, Kita 21, Nishi 10, Kita-ku, Sapporo, Hokkaido 001-0021, Japan

<sup>3 4</sup> Synfuels China Technology Co., Ltd., Beijing 101407, China

\* Corresponding authors.

E-mail: askr@cat.hokudai.ac.jp (K. Asakura); yzyuan@xmu.edu.cn (Y. Yuan).

## Abstract

It is always a long-term goal to investigate catalyst structure and stability for metal nitrides in catalytic reaction system. In our work, various metal nitrides are prepared and evaluated in the selective oxidation of alcohols. The  $\text{FeN}_x/\text{C}-T$  ( $T$  represents the pyrolysis temperature) catalysts display above 95% selectivity to aldehydes for the selective oxidation of unsaturated alcohols. The optimized  $\text{FeN}_x/\text{C}-900$  catalyst gives the highest TOF of  $7.0 \text{ h}^{-1}$  for the conversion of 5-hydroxymethylfurfural (HMF) to 2,5-diformylfuran (DFF). A combination study of characterizations and experiments suggests that Fe–N<sub>4</sub> species are the main active sites. In addition, we investigate the reasons for the catalyst deactivation and provide an effective approach to regenerate the catalysts. The results indicate that the deactivated catalysts can be regenerated by the heat treatment under an atmosphere of  $\text{NH}_3/\text{N}_2$ . Based on these studies, a plausible reaction mechanism is proposed over the  $\text{FeN}_x/\text{C}$  catalysts.

**Keywords:**  $\text{FeN}_x/\text{C}$  catalyst; Selective oxidation; Unsaturated alcohol; Stability; Regeneration

## 1. Introduction

In recent years, metal nitride catalysts have been developed rapidly in the fields of electrochemistry [1,2,3], catalytic oxidation [4,5,6] and organic synthesis [7] because of their unique structure properties. Metal nitride catalysts are often prepared by calcinating different precursors obtained from template methods [6,8], ball-milling [1,4] and oxidative polymerization [2,9]. Deng et al. reported a graphene supported FeN<sub>4</sub> (an iron moiety coordinated with four nitrogen groups) catalyst synthesized by ball-milling and calcination. It achieved the oxidation of benzene using H<sub>2</sub>O<sub>2</sub> as oxidant with 23.4% conversion and 18.7% yield of phenol at room temperature over 24 h [4]. Li and co-workers demonstrated that a N-doped graphene supported cobalt catalyst could convert benzyl alcohol to benzaldehyde in the atmosphere of O<sub>2</sub> with a yield of 92.4% after 5 h at 130 °C [5]. Xie et al. proposed a Fe–N–C catalyst using a template method, which was active for the oxidative dehydrogenation of 5-hydroxymethylfurfural (HMF) in aerobic solution with only a 40% yield of 2,5-diformylfuran (DFF) over 8 h at 80 °C under 1.0 MPa O<sub>2</sub> [8]. Quite recently, Liu et al. prepared atomically dispersed Fe–N–C catalysts by using MgO nanoparticles as the template and high temperature. It proved that the Fe–N–C-700 catalyst exhibited high activity for the selective oxidation of C–H bond using the *tert*-butyl hydroperoxide (TBHP) as an oxidant [6].

Despite the considerable studies of metal nitride, the structure of active sites and stability still deserve further investigation. The difficulties in investigating the active phases mainly lie in the complexities of structures and uncertainties of the catalyst compositions. There is no consensus on the active phase even efforts have been made in various research fields. Many researches have been conducted on active sites of iron-based nitrides for the oxygen reduction reaction (ORR) [1,10,11]. Artyushkova et al. proposed that a pyrrolic N species acted as the active site for O<sub>2</sub>

reduction to  $\text{H}_2\text{O}_2$  and that  $\text{Fe-N}_x$  species and pyridinic N atoms were the active sites for  $\text{H}_2\text{O}_2$  reduction to  $\text{H}_2\text{O}$  [10]. Choi and his co-workers reported that  $\text{FeN}_x\text{C}_y$  moieties were the main active sites for  $\text{H}_2\text{O}_2$  reduction [11]. Further, the recent work by Liu et al. discriminated the existence form of active sites in the  $\text{Fe-N-C}$  catalysts. They verified that  $\text{Fe}^{\text{III}}\text{-N}_5$  entity is the main active site for the selective oxidation of C-H bond with TBHP [6]. On the other hand, the stability of metal nitride catalysts has faced great challenges. The previous work proved that  $\text{Fe-N}_4$  and  $\text{Fe-N-C}$  catalysts deactivated in the oxidation reaction even at room temperature [4,8]. The deactivation phenomena also occurred in the ORR system [1,4,8,12,13]. Thus, it is very important to probe the essence of catalyst deactivation. A detailed study of deactivated catalyst will promote the development of methods to regenerate their performance.

It is well-known that the selective oxidation of alcohols is always a kind of important organic reaction that plays a great role in industrial applications, such as energy conversion and storage [14,15,16,17,18], the production of fine chemicals [15,17] and biomedical manufacturing [16,18]. Many catalysts have been reported for such reactions, such as supported nano-Au catalysts [19,20,21,22], supported nano-Pt, Pd, Ru catalysts [23,24,25,26,27], and other non-precious catalysts [28,29,30,31,32,33,34,35,36,37]. In this work, we prepared a series of metal nitrides ( $\text{MN}_x/\text{C-T}$ ,  $\text{M}=\text{Fe}$ ,  $\text{Co}$ ,  $\text{Cu}$ ,  $\text{Cr}$ , and  $\text{Ni}$ ) by a two-step pyrolysis treatment and employed for the selective oxidation of several alcohols by  $\text{O}_2$ , aiming to investigate the active phase, stability and regeneration of metal nitrides in the process of selective oxidation of alcohols. The results indicate that the  $\text{FeN}_x/\text{C-T}$  catalysts exhibit highest activity and selectivity for the conversion of unsaturated alcohols to the corresponding aldehydes by  $\text{O}_2$  as an oxidant. A  $\text{Fe-N}_4$  entity is identified as the main active phase for the  $\text{FeN}_x/\text{C-T}$  catalysts through a combination of XPS, ESR, EXAFS, control experiments and poisoning experiments with KSCN. In addition, efforts have been made to explore

the deactivation reason and the regeneration of metal nitrides catalysts.

## 2. Experimental

### 2. 1. Chemicals and reagents

Multiwalled carbon nanotubes (CNTs) and carbon black (XC-72 and Ketjen black EC-600JD) were purchased from Shenzhen Nanotech Port Co., Ltd. Ferric trichloride ( $\text{FeCl}_3 \cdot 6\text{H}_2\text{O}$ ), cobalt nitrate ( $\text{Co}(\text{NO}_3)_2 \cdot 6\text{H}_2\text{O}$ ), cupric nitrate ( $\text{Cu}(\text{NO}_3)_2 \cdot 3\text{H}_2\text{O}$ ), chromic nitrate ( $\text{Cr}(\text{NO}_3)_3 \cdot 9\text{H}_2\text{O}$ ), nickel nitrate ( $\text{Ni}(\text{NO}_3)_2 \cdot 6\text{H}_2\text{O}$ ) were obtained from Sinopharm Chemical Reagent Co., Ltd. HMF, DFF, and 2,5-furandicarboxylic acid (FDCA) were purchased from Aladdin Industrial Corporation (Aladdin<sup>®</sup>, Shanghai, China).

### 2. 2. Catalyst preparation

Commercial carbon materials, including CNTs, XC-72 and Ketjen black EC-600JD, were treated in  $\text{HNO}_3$  solution at 100 °C for 16 h. The  $\text{MN}_x/\text{C}-T$  ( $T$  represents the different pyrolysis temperatures) catalysts were prepared in a two-step pyrolysis process using *m*-phenylenediamine as the nitrogen source according to previous literature [2,9]. Briefly, *m*-phenylenediamine (3.0 g, 27.7 mmol) and the carbon support (Ketjen black EC-600JD, 0.4 g) were dispersed into a beaker containing a concentrated HCl aqueous solution. The suspension was stirred in the ice water bath, while the pre-cooled oxidant  $(\text{NH}_4)_2\text{S}_2\text{O}_8$  (2.0 M, 28 mL) was added slowly to oxidize *m*-phenylenediamine to cover the carbon support. After stirring for 24 h, the suspension solution was filtered, washed, and dried to obtain the N-doped carbon support. A series of metal salts ( $\text{FeCl}_3 \cdot 6\text{H}_2\text{O}$ ,  $\text{Co}(\text{NO}_3)_2 \cdot 6\text{H}_2\text{O}$ ,  $\text{Cu}(\text{NO}_3)_2 \cdot 3\text{H}_2\text{O}$ ,  $\text{Cr}(\text{NO}_3)_3 \cdot 9\text{H}_2\text{O}$ , and  $\text{Ni}(\text{NO}_3)_2 \cdot 6\text{H}_2\text{O}$ ) were used as precursors. The metal salt solution (0.3 M, 10 mL) was dropwise added into the dry N-doped

carbon support (1.2 g) dispersed in 20 mL of water. Then, the suspension was filtered and dried in an oven overnight at 100 °C before heat treatment. The obtained precursors were calcinated at different temperatures from 600–1000 °C for 1 h in a nitrogen atmosphere. Subsequently, the pyrolyzed samples were leached in HCl solution (1 M, 100 mL) at 80 °C for 8 h to remove impurities, such as  $MC_x$ ,  $MO_x$  and  $MS_x$ , from the sample and washed to neutralize the samples using deionized water. Finally, the samples were calcinated again in the same atmosphere and temperature for 3 h to form the corresponding  $FeN_x/C-T$ ,  $CoN_x/C-T$ ,  $CuN_x/C-T$ ,  $CrN_x/C-T$ , and  $NiN_x/C-T$  catalysts. Similarly,  $FeN_x/CNT-T$  and  $FeN_x/XC72-T$  were synthesized by changing the carbon supports.  $FeN_x/C-700^*$  and  $FeN_x/C-600^*$  with same N amount as  $FeN_x/C-900$  were also obtained by controlling the amount of nitrogen source. Briefly, other conditions remain unchanged only decreasing the amount of *m*-phenylenediamine to 0.2 g and 0.15 g for  $FeN_x/C-700^*$  and  $FeN_x/C-600^*$  respectively.  $M/C-T$  and  $CN_x-T$  were prepared using the method similar to  $MN_x/C-T$  without the addition of the nitrogen source and metal salt precursor, respectively.

### 2. 3. Catalyst characterization

The porous properties of the catalysts were analyzed by  $N_2$  adsorption-desorption measurements at  $-196$  °C using a Micromeritics Tristar II 3020 apparatus. The catalysts were degassed at 100 °C for 4 h under vacuum treatment before the measurements. The specific surface area was calculated through the Brunauer-Emmett-Teller (BET) method. The average pore diameter of the catalysts was determined by the Barret-Joyner-Halenda (BJH) desorption isotherm. Powder X-ray diffraction (XRD) analysis was carried out on a PANalytical X'pert Pro diffractometer equipped with Cu- $K_\alpha$  radiation ( $\lambda = 1.5418$  Å) at a scanning rate of 20 °/min from 10° to 90°.

Raman spectra were collected on a Renishaw Invia Raman microscope with the CCD detector. The Raman data were recorded using a 532 nm excitation by a He–Cd laser source with a time of 10 s exposure. The output power of the laser was 13 mW.

Transmission electron microscopy (TEM) and high angle annular dark-field scanning transmission electron microscopy (HAADF-STEM) images were taken on a transmission electron microscope (TECNAI F30). The acceleration voltage was 300 kV. The catalysts were ground and ultrasonically dispersed in ethanol before observation. The suspension was dropped onto a copper grid supported by super thin carbon films.

The metal content of the catalysts was obtained by a XRF spectrometer (BRUKER) at 60 kV and 50 mA. Before the measurements, the catalysts were mixed with boric acid ( $\text{H}_3\text{BO}_3$ ) and then pressed into 2 mm pellets. The contents of C, N and H elements were measured by elemental analysis on an Elementar Vario EL III instrument.

X-ray photoelectron spectroscopy (XPS) was performed on a Qtac-100 LEISS spectrometer with an Al  $K_\alpha$  incident radiation source. The C1s peak (284.6 eV) was referenced to calibrate the binding energies of the catalysts.

Electron spin resonance (ESR) spectra were recorded on an X-band Bruker EMX-10/12 apparatus at  $-173\text{ }^\circ\text{C}$ . The samples (20 mg) were poured into quartz tubes and cooled to  $-173\text{ }^\circ\text{C}$  in the liquid nitrogen atmosphere. The experimental frequency was 9.45 GHz, and the operating power was 19.94 mW.

X-ray absorption fine structure (XAFS) was carried out at BL9C of the Photon Factory, Institute for Materials Structure Science, High Energy Accelerator Research Organization (KEK-IMSS-PF), Japan (Proposal No. 2016G546). The X-rays were monochromatized by a Si(111) double-crystal. The XAFS spectra were collected at room temperature. Higher harmonics were

rejected by a total reflection focusing mirror. The ionization chambers for the incident X-rays (IO) and the transmitted X-rays (I) were both filled with N<sub>2</sub>. The REX program was used to analyze the EXAFS spectra ( $\mu(E)$ ) [38,39,40]. The smoothed background ( $\mu_s(E)$ ) was estimated by a smoothing spline method and normalized by the edge height ( $\mu_0(E)$ ), whose energy dependence was calculated using McMaster equation. The energy scale was converted to wavenumbers,  $k$ , using the following equation:

$$k = \sqrt{2m(E - E_0)/\hbar^2}$$

where  $E_0$  is absorption edge energy.

Thus, the obtained EXAFS oscillation ( $\chi(k)$ ) was weighted by  $k^3$  and Fourier transformed. The peaks were filtered and inversely Fourier transformed for further curve fitting analysis in  $k$ -space. The curve fitting analysis was carried out using the following equations:

$$k^3\chi(k) = \sum_i \frac{S_i N_i F_i(k)}{k r_i^2} \exp(-2k^2 \sigma_i^2) \exp\left(-\frac{2r_i}{\lambda_i}\right) \sin(2kr_i + \phi_i(k))$$

$$\chi(k) = \frac{\mu(E) - \mu_s(E)}{\mu_0(E)}$$

where  $S_i$ ,  $r_i$ ,  $N_i$ ,  $\sigma_i$ , and  $\lambda_i$  are the inelastic loss factor, bond distance, coordination number, Debye-Waller factor, and mean free path of the  $i$ -th bonds, respectively. The values of  $r_i$ ,  $N_i$ ,  $\sigma_i$  and  $E_0$  were determined by curve fitting analysis. The value of  $\lambda_i$  was fixed at 7 Å and that of  $S_i$  was determined by standard compounds. The phase shift  $\phi_i(k)$  and amplitude function  $F_i(k)$  were derived using the FEFF program [41,42].

#### 2. 4. Catalytic test

Selective oxidation experiments of various alcohols were conducted in a high-pressure reactor. A series of alcohols (benzyl alcohol (99.5%), furfuralcohol (98.0%), HMF (99.0%), 5-methyl-2-

furyl-methanol (97.0%), 2,5-furandimethanol (97%), cyclohexanol (98.5%), glycerol (99.0%), and ethanol (99.5%)) were used as reactants.

The selective oxidation of various alcohols was carried out in a 50 mL stainless steel autoclave. Typically, alcohol (0.25 mmol, except for 2,5-furandimethanol, 0.125 mmol), the catalyst (0.1 g), and DMF (10 mL) were loaded in the reactor. Then the reactor is filled with O<sub>2</sub> (0.5 MPa) as an oxidant for a certain period of time at 500 rpm stirring speed. It took approximately 14 min to reach the reaction temperature. At the end of the reaction, the reactor was immediately immersed in ice water, and subsequently, O<sub>2</sub> was released to terminate the reaction. For the selective oxidation of HMF, the reaction liquid sample was filtered and analyzed by high-performance liquid chromatography (HPLC) on a Shimadzu LC-20A instrument with a Shodex Sugar column and a refractive index detector. The mobile phase was a 0.5% H<sub>2</sub>SO<sub>4</sub> aqueous solution. For the selective oxidation of the other alcohols, the liquid products were analyzed by gas chromatography on an Agilent 7890A with an HP-5 column and a flame ionization detector. The conversion of alcohols and the selectivity of the products were acquired on a carbon basis.

The Weisz-Prater criterion ( $C_{WP}$ ) was calculated to eliminate the mass transfer limitations according to the references [43,44].

$$C_{WP} = \frac{-r'_A \rho_c R^2}{D_e C_{As}}$$

where,  $-r'_A$  = reaction rate, kmol/kg-cat · s;  $R$  = catalyst particle radius, m;  $\rho_c$  = solid catalyst density, kg/m<sup>3</sup>, here,  $\rho_c = 800$  kg/m<sup>3</sup>;  $D_e$  = effective diffusivity coefficient, m<sup>2</sup>/s;  $C_{As}$  = gas concentration of A at the catalyst surface, kmol-A/m<sup>3</sup>.

The carbon balance of the reaction was obtained by using the known compounds for calibration. All the catalysts gave a carbon balance above 97.0%. Because the low loading and high dispersion of Fe, we measured the turnover frequency (TOF) on the total Fe metal atoms determined from by XRF, indicating the moles of HMF converted by per Fe atom on the catalyst

per hour ( $\text{mol-HMF mol-Fe}^{-1} \text{ h}^{-1}$ , for short,  $\text{h}^{-1}$ ). The HMF conversion for the TOF calculation in all case was below 10%. The carbon balance and TOF were calculated by the equations as follows:

$$\text{Carbon balance} = \frac{\text{Total moles of carbon in products}}{\text{Moles of carbon in substrate}}$$

$$\text{TOF} = \frac{\text{Moles of HMF converted}}{\text{Fe atoms} \times \text{Time}}$$

The KSCN titration experiment was performed to quantify the active sites. Prior to the reaction, the catalyst (22 mg) and specified equivalent of KSCN solution (1.4 mg/mL) were mixed in the reaction. After stirring for 1 h, the HMF (25 mg) and  $\text{O}_2$  (0.5 MPa) were added to the reaction system and heat to 100 °C in 14 minutes. Theoretically, the mole number of KSCN was considered as the content of active sites. The TOF were calculated based KSCN titration experiment by the equations as follows:

$$\text{TOF} = \frac{\text{Converted HMF molecules}}{\text{Active sites} \times \text{Time}}$$

Where, the data of converted HMF molecules were calculated through multiplying the mole of HMF input with the HMF conversion difference with and without KSCN; the active sites were determined by the amount of KSCN when the DFF yield remained almost constant.

To determine the recyclability of  $\text{MN}_x/\text{C-T}$ , the used catalysts were recovered by centrifugation, washed and dried in an oven at 100 °C overnight without further treatment. To evaluate the activities of the regenerated catalysts, the used catalysts were heat treated in a  $\text{N}_2$  or  $\text{NH}_3/\text{N}_2$  atmosphere for 1 h.

### 3. Results and discussion

#### 3. 1. Structural property of $\text{FeN}_x/\text{C-T}$

The textural properties and features of FeN<sub>x</sub>/C-*T* were investigated using a battery of characterizations. The XRD patterns showed that the FeN<sub>x</sub>/C-*T* catalysts from different pyrolysis temperatures had the same diffraction lines (Fig. S1). Only two peaks (24.8° and 43.7°) were observed, assigning to the diffractions of graphite from the carbon support [2,24]. There were no any diffraction peaks attributed to Fe-containing crystalline phases, which indicated that no large particles existed in the FeN<sub>x</sub>/C-*T* catalysts. The surface area and pore size distribution data of the FeN<sub>x</sub>/C-*T* samples by N<sub>2</sub> adsorption-desorption measurements were listed in Table S1. The specific surface area of the catalysts increased from 403 to 901 m<sup>2</sup>/g with the increase of pyrolysis temperature. The average pore size ranged from 4.2 to 5.1 nm with a feature of mesoporous materials. The Raman spectra indicated that the integrated intensity ratio of the D band at 1340 cm<sup>-1</sup> and the G band at 1590 cm<sup>-1</sup> (*I*<sub>D</sub>/*I*<sub>G</sub>) increased in a range of 1.38–1.55 with increasing pyrolysis temperature (Fig. S2). This indicated that a higher pyrolysis temperature created more structural defects on the carbon supports [45,46].

To identify the dispersion states and morphologies of the Fe species in the FeN<sub>x</sub>/C-*T*, TEM and HAADF-STEM measurements were performed. In the bright-field images of FeN<sub>x</sub>/C-*T*, no crystalized Fe species were observed (Fig. 1a, b and S3), which is in good agreement with the results from the XRD pattern analyses. In the dark-field images of FeN<sub>x</sub>/C-900 catalyst, a little Fe species were identified (Fig. 1b). STEM mapping showed the Fe species were integrated tightly with the C and N elements (Fig. 1d).

There was a small difference in Fe content in the five catalysts as indicated in Table 1, that is, 1.31% for FeN<sub>x</sub>/C-1000, 0.9% for FeN<sub>x</sub>/C-900, 1.1% for FeN<sub>x</sub>/C-800, 1.38% for FeN<sub>x</sub>/C-700 and 0.89% for FeN<sub>x</sub>/C-600. The N content of the catalysts critically depended on the pyrolysis temperature. Among them, the N content in the FeN<sub>x</sub>/C-900 was 4.3%, which was higher than 2.7%

for FeN<sub>x</sub>/C-1000 and lower than 7.4% for FeN<sub>x</sub>/C-800, 10.7% for FeN<sub>x</sub>/C-700 and 14.4% for FeN<sub>x</sub>/C-600.

### 3. 2. Selective oxidation of alcohols over FeN<sub>x</sub>/C-T catalyst

We performed a series of experiments with the MN<sub>x</sub>/C-900 catalysts for the selective oxidation of HMF. The results showed only FeN<sub>x</sub>/C-900 and CrN<sub>x</sub>/C-900 could afford 100% and 88.6% selectivity to DFF under the same reaction conditions; other MN<sub>x</sub>/C-900 catalysts, such as CoN<sub>x</sub>/C-900, CuN<sub>x</sub>/C-900, and NiN<sub>x</sub>/C-900, displayed lower activity or worse selectivity (Fig. S4). We then evaluated the influence of FeN<sub>x</sub> catalysts with different carbon supports on the catalytic performance. It indicated that these catalysts gave quite good HMF conversions, 51.6% for FeN<sub>x</sub>/C-900, 61.4% for FeN<sub>x</sub>/CNT-900 and 54.4% for FeN<sub>x</sub>/XC72-900, with 100% selectivity to DFF over 1 h of reaction (Fig. S5). Based on the above experiments, we considered that carbon support no matter of its structure was a type of quite good carrier for the FeN<sub>x</sub> catalysts and that a specific metal center was needed for the selective oxidation of HMF. Therefore, we focus on the structure-performance correlation of FeN<sub>x</sub>/C-T catalysts in the following studies.

In the selective oxidation of HMF, all the FeN<sub>x</sub>/C-T catalysts exhibited 100% selectivity to DFF without the formation of FDCA with 0.5 MPa O<sub>2</sub> at 100 °C. However, the HMF conversion increased from 6.9% to 51.6% then dropped to 34% with an increasing pyrolysis temperature from 600–1000 °C. FeN<sub>x</sub>/C-800 and FeN<sub>x</sub>/C-900 displayed similar catalytic behaviors (Fig. 2). It indicated the high specific area of FeN<sub>x</sub>/C-T was not good standard for high catalytic activity. The concentration of active species was essential. The excessive high treatment temperature (for example 1000 °C) could not generate high density of active species. Thus, the decrease of HMF conversion at 1000 °C was caused by the loss of active species. The TOF and reaction rate based

on total Fe atoms were summarized in Fig. 3 and Table S2. The reaction rates of FeN<sub>x</sub>/C-900 and FeN<sub>x</sub>/C-800 for the HMF selective oxidation were similar to each other (approximately 1.1–1.4 × 10<sup>-3</sup> mol·g<sub>cat</sub><sup>-1</sup>·h<sup>-1</sup>). The TOF values over FeN<sub>x</sub>/C-900 and FeN<sub>x</sub>/C-800 were 7.0 h<sup>-1</sup> and 5.9 h<sup>-1</sup>, respectively, which were 2–3 times higher than FeN<sub>x</sub>/C-700 and FeN<sub>x</sub>/C-1000. Because the Fe amount in FeN<sub>x</sub>/C-*T* are almost the same based on Table 1, The difference of TOF was caused by the amount of active species. To precisely explore the intrinsic activity of catalysts, the KSCN titration experiment was performed because SCN<sup>-</sup> could bond with Fe-centered species and deactivate them [2,6,47,48]. The TOF based on KSCN titration experiment was listed in the Table S3. The TOF values of FeN<sub>x</sub>/C-900 and FeN<sub>x</sub>/C-800 were 23.5 h<sup>-1</sup> and 17.4 h<sup>-1</sup> respectively. It is 3 times higher than TOF obtained on bulk composition of Fe. When the amount of KSCN was 0.2 equivalent of Fe content in the FeN<sub>x</sub>/C-*T*, the conversion of HMF almost remained constant. It indicated the Fe content in the FeN<sub>x</sub>/C-*T* was similar, which consistent with the results of XRF in Table 1 and the FeN<sub>x</sub>/C-900 and FeN<sub>x</sub>/C-800 had high density of active sites. This results proved that the N doped carbon also contribute to the catalytic activity, which was in line with the following experiment (Fig. S6). Compared with the results reported in the previous literature [8,26,27,28,30,31,33], the catalytic activity of FeN<sub>x</sub>/C-900 was comparable to the noble catalyst. Among a series of non-precious catalysts, FeN<sub>x</sub>/C-900 had higher TOF with lower loading of metal under the mild reaction conditions. (Table S4).

For FeN<sub>x</sub>/C-900, we systematically investigated the time course for the product distribution of HMF oxidation. Prolonging the reaction time to 5 h, the conversion of HMF reached 96.2%, and the selectivity to DFF slightly decreased from 100% to 98.9%, accompanying the formation of FDCA. Further prolonging the reaction time to 10 h, HMF was almost completely converted, and the selectivity to DFF dropped to 97.3% (Fig. 4). Through analysis of the time-course results,

we found that FeN<sub>x</sub>/C-900 could effectively restrain the excessive oxidation of DFF.

We further gained insight into the effects of the reaction time, stirring speed, reaction temperature and catalyst amount on the activities of FeN<sub>x</sub>/C-*T* (Tables S5, S6 and S7). Based on the experimental data, for FeN<sub>x</sub>/C-800 and FeN<sub>x</sub>/C-900, the yield of DFF reached above 90% by prolonging the reaction time. Taking the FeN<sub>x</sub>/C-900 catalyst for an example, even with a reduced reaction temperature to 60 °C, the conversion of HMF reached 61.7% with a prolonged reaction time of 16 h. Meanwhile, the yield of DFF increased from 28.5% to 51.6% after 1 h by decreasing the mole ratio of HMF to Fe from 30 to 15 for FeN<sub>x</sub>/C-900. Compared to FeN<sub>x</sub>/C-800 and FeN<sub>x</sub>/C-900, the HMF conversion over FeN<sub>x</sub>/C-700 was only 48.2%, and the selectivity to DFF remained high (97.3%) after 8 h of reaction at 100 °C with 0.5 MPa O<sub>2</sub>. The results indicated that a prolonged reaction time could not enhance the activity of FeN<sub>x</sub>/C-700. As for FeN<sub>x</sub>/C-900, the catalytic activity of FeN<sub>x</sub>/C-900 remained constant by changing the stirring speed from 300 rpm to 800 rpm, meanwhile, C<sub>WP</sub> gave  $1.6 \times 10^{-15} < 1$  (see supplementary information). It indicated no internal diffusion limitations in the reaction systems.

To further testify the selective oxidation abilities of FeN<sub>x</sub>/C-900, we chose several alcohols with typical structures as substrates. As shown in Table 2, FeN<sub>x</sub>/C-900 exhibited extraordinary selective oxidation performance for various unsaturated monohydric alcohols containing β-H with above 97% selectivity to the corresponding aldehydes in high conversions (Table 2, entries 1–4). Dihydric alcohol was also smoothly transformed into the dialdehyde with 81.5% selectivity in 99.3% conversion (Table 2, entry 5). However, in the oxidation process of cyclohexanol, only 16.6% conversion with 38.8% selectivity to cyclohexone was obtained after 10 h at 100 °C, companying some polymerization products of cyclohexanone and DMF based on the GC-MS analysis. (Table 2, entry 6). For the selective oxidation of aliphatic alcohols, no products were detected on FeN<sub>x</sub>/C-

900 (Table 2, entries 7 and 8).

We are very curious on the origin behind the excellent performance of FeN<sub>x</sub>/C-900 catalyst. A series of control experiments have been carried out to try to understand the essence as shown in Fig. S6. Under the same reaction conditions, the HMF conversion was 2.9% with 36.7% selectivity to DFF and 63.3% selectivity to FDCA on the Fe/C-900 catalyst. When the reaction was carried out on the CN<sub>x</sub>-900 catalyst, the conversion of HMF was 11.3% with 93.4% selectivity to DFF and 6.6% selectivity to FDCA. There was no formation of DFF in the blank experiment. This proved that N doped carbon also contribute to the activity. Considering that there are plentiful N doped carbon species ( $n_N/n_{Fe}=19:1$ ) in FeN<sub>x</sub>/C-900 catalyst, we can conclude that the Fe–N sites are more active than N doped carbon sites.

### 3. 3. Chemical state, active phase and coordination environment of FeN<sub>x</sub>/C-*T*

#### 3. 3. 1. Chemical state and active phase of FeN<sub>x</sub>/C-*T*

In order to further prove the active phase of FeN<sub>x</sub>/C-*T*, based on the above experiment results, we measured the N 1s XPS profiles of several FeN<sub>x</sub>/C-*T* catalysts as shown in Fig. 5. According to the results in literature [10,49,50,51,52], the N 1s data were deconvoluted into five peaks which were categorized as cyano N (–CN), pyridinic N, Fe–N, pyrrolic N, and graphitic N, respectively. The curve fittings were performed by fixing the binding energy position of corresponding N species with a full-width-half-maximum as 1.4 eV for each peak (Table S8) [10,49,50,51,52]. The assignment and position as well as the corresponding content of these peaks are summarized in Tables S8, S9 and S10, respectively. The effective concentration of Fe–N species increased in the following order: FeN<sub>x</sub>/C-800 > FeN<sub>x</sub>/C-900 > FeN<sub>x</sub>/C-600 > FeN<sub>x</sub>/C-700 > FeN<sub>x</sub>/C-1000. The FeN<sub>x</sub>/C-800 and FeN<sub>x</sub>/C-900 catalysts had the largest concentration of Fe–N, which is in line with

their catalytic activity as shown in Fig. 2. However, the FeN<sub>x</sub>/C-1000 catalyst possessed the lowest concentration of Fe–N species but it shown an activity more than that of FeN<sub>x</sub>/C-700 and 600.

To accurately prove whether Fe–N is an important active phase, we prepared another two catalysts, namely FeN<sub>x</sub>/C-700\* and FeN<sub>x</sub>/C-600\*, to maintain a similar N content N content as FeN<sub>x</sub>/C-900 (Table S11). In this case, the average N contents in the bulk catalysts are similar but the concentration of N-containing species are quite different under different pyrolysis temperature, which can exclude the effect of some unavailable N species and is beneficial for the investigation of active species. The catalytic activities were evaluated in the selective oxidation of HMF, and the results are listed in Fig. 6. Compared to FeN<sub>x</sub>/C-900, FeN<sub>x</sub>/C-600 and FeN<sub>x</sub>/C-700, the DFF selectivity reduced to 73.7% for FeN<sub>x</sub>/C-600\* and 68.2% for FeN<sub>x</sub>/C-700\* at 3.9% and 8.9% conversions of HMF, respectively. To probe the origins, XPS measurements were carried out. Fig. S7 illustrates the N 1s XPS spectra of FeN<sub>x</sub>/C-900, FeN<sub>x</sub>/C-600 and FeN<sub>x</sub>/C-600\*. The distribution of different N species is listed in Table S12. The effective concentration of Fe–N species was 16.9% in FeN<sub>x</sub>/C-900, and decreased to 6.6% in FeN<sub>x</sub>/C-600\*. Based on the above results, we considered that the Fe–N species were the key to high catalytic activity and selectivity for the reaction. Furthermore, the N content might have an important influence on the catalytic performance.

### 3. 3. 2. Coordination environment of FeN<sub>x</sub>/C-*T*

To further investigate relationship between activity of the catalyst and the presence of Fe species the ESR was measured to research the states and coordination structures of Fe species catalysts. Fig. 7 displays the ESR spectra of the five FeN<sub>x</sub>/C-*T* catalysts. There were two signals at  $g \sim 2.0$  and  $g \sim 4.3$  over the entire magnetic field. The ESR signal at  $g \sim 4.3$  originated from isolated Fe<sup>3+</sup> species in tetrahedral and distorted tetrahedral coordination environments such as

rhombic and tetragonal symmetry [53,54,55,56,57]. The Shelef and Vasiliev groups assigned the signal at  $g \sim 2.0$  to ferric species arising from the aggregate structure (dimer and trimer) [54,58,59].

For the five catalysts, an increase of the calcination temperature from 600 °C to 1000 °C is accompanied by the change in the intensities of the ESR lines at the  $g \sim 2.0$  and  $g \sim 4.3$  regions. The intensity of the signal at  $g \sim 2.0$  decreased with an increasing pyrolysis temperature. It indicated that the agglomerated Fe species were unstable at high temperature [54]. In contrast, the intensity for the signal catalysts first increased at the  $g \sim 4.3$  region with the form 600–900 °C, which indicates an increase of the tetrahedral coordinated Fe sites [54]. However, when the treatment temperature increased to 1000 °C, the intensity of  $g \sim 4.3$  signal in FeN<sub>x</sub>/C-1000 was lower than FeN<sub>x</sub>/C-900. The results are consistent with the XPS analysis, which proved excessively high temperature (1000 °C) could not promote the formation of active sites. To eliminate the influence of signal-to-noise ratio, plots of ESR intensity ratio of signals at  $g \sim 4.3$  and  $g \sim 2.0$  ( $I_{4.3}/I_{2.0}$ ) versus pyrolysis temperature are shown in Fig. S8. It can be found that the  $I_{4.3}/I_{2.0}$  ratio increased rapidly with the increase of pyrolysis temperature from 600 °C to 900 °C. Although it is hard to quantify the concentration of active species, but it is clear that with increasing pyrolysis temperature the signal at  $g \sim 4.3$  increased and the signal at  $g \sim 2.0$  decreased respectively. Additionally, the Fe contents over all catalysts were almost the same based on XRF, which suggested an increase of active species and reached max at FeN<sub>x</sub>/C-900 and FeN<sub>x</sub>/C-800. Based on these analysis results, we can conclude that catalytic activity was not only related to density of Fe–N species but also depended on the chemical state of Fe–N species. The agglomerated Fe species had negative effect on the catalytic activity and the isolated coordination Fe species might be the main active phase.

To gain deep insight into the coordination environments and chemical states of the Fe species

in the FeN<sub>x</sub>/C-*T* catalysts, the four FeN<sub>x</sub>/C-*T* samples were subjected to X-ray absorption fine structure (XAFS) spectroscopy. Fig. 8A shows the Fe K-edge XAFS spectra of the four FeN<sub>x</sub>/C-*T* samples. The pre-edge structures of the FeN<sub>x</sub>/C-*T* samples were nearly the same, indicating the presence of an inversion center or octahedral structure. The Fe K-edge positions showed no considerable shifts among the 4 samples. The edge positions are shown in Fig. 8A, revealing a 2.0 eV shift with an increasing treatment temperature, and the edge position is similar to that of Fe<sub>2</sub>O<sub>3</sub> (7125.9 eV). Thus, Fe<sup>3+</sup> species predominantly existed in FeN<sub>x</sub>/C-900. Fig. 8B displays the Fourier transforms of the *k*<sup>3</sup> EXAFS spectra of the corresponding catalysts. The Fourier transform range between 3 and 12 Å<sup>-1</sup> is depicted in Fig. S9. As shown in Fig. 8B, the first peak at 1.53 Å for FeN<sub>x</sub>/C-800 and 900 corresponds to the Fe–N bonds [54]. The fitting results of the EXAFS are listed in Table S13. The EXAFS oscillations for the low-temperature treated samples damped quickly, and the Debye-Waller factor became large. The coordination number for the first shell of FeN<sub>x</sub>/C-800 and 900 was approximately 4.0 (3.9 ± 0.2 for FeN<sub>x</sub>/C-800 and 3.8 ± 0.2 for FeN<sub>x</sub>/C-900 respectively), indicating the formation of a Fe–N<sub>4</sub> species. The results are in accordance with the analysis of ESR and XPS. The second shell appearing in FeN<sub>x</sub>/C-800 and FeN<sub>x</sub>/C-900 at 2.9 Å can be assigned to the contribution of Fe–N–C. The peaks at 2.1 Å in the catalysts should be Fe–Fe bond. As for FeN<sub>x</sub>/C-600 and FeN<sub>x</sub>/C-700, their spectra showed a little different structure with much more disorder. Thus, it was difficult to determine the structure of FeN<sub>x</sub>/C-600 and FeN<sub>x</sub>/C-700 in details. FeN<sub>x</sub>/C-700 featured a mixture of the active phase appearing in FeN<sub>x</sub>/C-900 and the precursor state of FeN<sub>x</sub>/C-600, resulting in the EXAFS oscillations reducing by the interference of the different structures. In summary, the EXAFS results proved that FeN<sub>x</sub>/C-800 and 900 possessed Fe–N<sub>4</sub>-like species.

### 3. 4. Deactivation and regeneration of FeN<sub>x</sub>/C-T

Attaining catalytic stability is always a great challenge for FeN<sub>x</sub>/C-T catalysts [1,4,8,12,13]. More detailed works are needed to focus on this aspect. Our study investigated the reasons behind deactivation after the initial high catalytic performance and made an effort to effectively regenerate the catalyst structure and its performance.

The stability of the FeN<sub>x</sub>/C-900 catalyst has been investigated carefully, and the results are summarized in Table S14 and Fig. 9. After the second recycling experiment without any treatment to FeN<sub>x</sub>/C-900, the HMF conversion dropped to 23.4%, and only approximately a quarter of the initial activity of the first run was maintained. The selectivity to DFF also reduced from 99.1% to 84.4% (Table S14, entry 2). However, after heat treatment of used FeN<sub>x</sub>/C-900 at 900 °C in a N<sub>2</sub> atmosphere for 1 h, the HMF conversion increased to 96.7% with 99.4% selectivity to DFF (Table S14, entry 3). Prolonging the heat treatment time to 3 h, the HMF conversion only increased to 84.7%, and the DFF selectivity remained 99.4% (Table S14, entry 4). Fig. 9a presents that the stability performance of regenerated catalyst by calcination at a N<sub>2</sub> atmosphere for 1 h. The catalytic activity began to reduce again after 3 recycles. The yield of DFF reduced to 72.1% after 6 runs. However, we changed the regeneration atmosphere to 3% NH<sub>3</sub>/N<sub>2</sub> after 3 runs. The yield of DFF was maintained at approximately 90% after 6 runs in Fig. 9b.

To reveal the reasons behind the deactivation and regeneration, the used and regenerated FeN<sub>x</sub>/C-900 catalyst was characterized by N<sub>2</sub> adsorption–desorption measurement, elemental analysis and ESR spectroscopy. Fig. S10 shows the ESR spectra of the FeN<sub>x</sub>/C-900 catalyst in different conditions. For the used FeN<sub>x</sub>/C-900 catalyst, an ESR signal at  $g\sim 2.0$  appeared, suggesting the formation of aggregated iron species. The decreased signal intensity at  $g\sim 4.3$  indicated the loss of tetrahedral coordinated Fe sites. It showed that active Fe species in the

FeN<sub>x</sub>/C-900 catalyst aggregated in the reaction. The specific area of FeN<sub>x</sub>/C-900 after reaction decreased, indicating the happen of Fe species aggregation (Table S15). For the regenerated FeN<sub>x</sub>/C-900 catalyst, the ESR signal at  $g\sim 2.0$  did not appear, and the intensity of the ESR line at  $g\sim 4.3$  slightly increased. The results showed that the active Fe sites could regenerate in the heat treatment process without the formation of aggregated Fe species [54]. Thus, the agglomeration of Fe species and the loss of active Fe sites in the used FeN<sub>x</sub>/C-900 catalyst were the main reasons for catalyst deactivation.

Table S16 lists the results of elemental analysis. After heat treatment, the N content of FeN<sub>x</sub>/C-900 catalyst was reduced. For the FeN<sub>x</sub>/C-900 catalyst treated in a N<sub>2</sub> atmosphere, the N content was only  $\sim 1\%$  after 6 runs (Table S16, entry 4). For the FeN<sub>x</sub>/C-900 catalyst treated in an NH<sub>3</sub>/N<sub>2</sub> atmosphere, the loss of N content was depressed. After 6 runs, the N content was maintained at  $\sim 2\%$  (Table S16, entry 7). The supplement of N element might be an important method to effectively regenerate the Fe–N<sub>4</sub> structure and its performance.

### 3. 5. Catalytic mechanism of FeN<sub>x</sub>/C-T

In the selective oxidation of alcohols, the FeN<sub>x</sub>/C-T catalysts exhibited high selectivity to the corresponding aldehydes, and the main active sites were Fe–N<sub>4</sub> species. The experimental results proved that the incorporation of N atoms suppressed the formation of FDCA and promoted the selectivity to the corresponding aldehyde (Fig. S6). It is important to note that the doped N was the only reason to regulate the selectivity. Previous works have reported that doping with nitrogen groups offered coordinating sites for metal ions to generate the reactive phase for the reduction of O<sub>2</sub> [1]. Many references in the electrochemical field had proved that Fe–N–C catalysts can effectively promote reduction of O<sub>2</sub> [1,2,9,13,47]. Fe–N species could activate adsorbed molecular

O<sub>2</sub> to create peroxy or superoxy oxygen species by donating electrons [2,9,10,60]. On the other hand, EXAFAS proved the coordination number of N to Fe atom is approximately 4, indicating the catalysts was unsaturated coordination structure. It is validated that this structure had catalytic activity in the oxidation reaction systems [4,6]. Meanwhile, It also proved Fe–N–C had high catalytic activity toward oxidation of H<sub>2</sub>O<sub>2</sub> and heterocyclic compound [2,6,61]. Combining our work with previous reports, a possible and plausible reaction mechanism was proposed to explain the selective oxidation of alcohols in Scheme 1.

In the reaction process, molecular O<sub>2</sub> was adsorbed on the Fe–N<sub>4</sub> active sites. It has been reported that the incorporation of N atoms enhanced the electronic density of the active sites [62]. Thus, an electron transferred from the Fe–N<sub>4</sub> active sites to adsorbed O<sub>2</sub>. After accepting the electron, the adsorbed O<sub>2</sub> became a peroxy species (-O–O-). After that, the proton H on the alcoholic hydroxyl group transferred to the N<sup>δ-</sup> species of the Fe–N<sub>4</sub> sites, and meanwhile, the O<sup>δ-</sup> of the hydroxy group interacted with the Fe<sup>δ+</sup> sites of the Fe–N<sub>4</sub> active phase. Then, the β–H of the unsaturated alcohol transferred to the peroxy species to form H<sub>2</sub>O, similar to the ORR mechanism on FeN<sub>x</sub>/C-*T* [10,60] and the corresponding aldehyde was released from the active sites.

#### 4. Conclusions

In conclusion, a series of MN<sub>x</sub>/C-*T* catalysts are prepared by a two-step pyrolysis method. Their catalytic performances are evaluated in the selective oxidation of various alcohols. The FeN<sub>x</sub>/C-*T* catalysts obtained at different pyrolysis temperatures show promising selectivity to the corresponding aldehydes for the selective oxidation of unsaturated alcohols. Particularly, the catalyst FeN<sub>x</sub>/C-900 can perform the selective oxidation of HMF to DFF with almost complete

conversion and selectivity higher than 97% under the optimized conditions. A combination study including elemental analysis, XPS, ESR spectroscopy, HAADF-STEM, and EXAFS verify that the main active site is Fe–N<sub>4</sub> sites, and the concentration of Fe–N<sub>4</sub> species and the state of ferric species are very important factors for the catalytic performance. The higher Fe–N<sub>4</sub> concentration with more isolated ferric species, the higher activity for the selective oxidation of HMF to DFF. A plausible reaction mechanism based on Fe–N<sub>4</sub> active sites is thus proposed. Moreover, we explain that the reason causing catalyst deactivation is essentially due to the loss of effective N species by ESR measurements. The results demonstrate that the activity of FeN<sub>x</sub>/C-900 catalyst can be regenerated by heat treatment under the atmosphere of NH<sub>3</sub>/N<sub>2</sub>. To close, the present findings into the structures of FeN<sub>x</sub>/C catalysts and their catalytic performances with molecular O<sub>2</sub> may shed new light on the design and understanding of such emerging transition-metal hydrides for various catalytic applications.

## **Acknowledgments**

We acknowledge the financial support from the National Key R&D Program of China (2017YFA0206801), the National Natural Science Foundation of China (91545115 and 21473145), and the Program for Innovative Research Team in Chinese Universities (IRT\_14R31).

## **Appendix A. Supplementary material**

Supplementary data associated with this article can be found, in the online version, at <https://doi.org/10.1016/j.jcat.2018.xx.xxx>.

## **References**

- [1] M. Lefèvre, E. Proietti, F. Jaouen, J.P. Dodelet, Iron-based catalysts with improved oxygen reduction activity in polymer electrolyte fuel cells, *Science* 324 (2009) 71-74.
- [2] Q. Wang, Z.Y. Zhou, Y.J. Lai, Y. You, J.G. Liu, X.L. Wu, E. Terefe, C. Chen, L. Song, M. Rauf, N. Tian, S.G. Sun, Phenylenediamine-based FeN(x)/C catalyst with high activity for oxygen reduction in acid medium and its active-site probing, *J. Am. Chem. Soc.* 136 (2014) 10882-10885.
- [3] K. Artyushkova, C. Walker, W. Patterson, P. Atanassov, Hierarchically structured non-PGM oxygen reduction electrocatalyst based on microemulsion-templated silica and pyrolyzed iron and cyanamide precursors, *Electrocatalysis* 5 (2014) 241-247.
- [4] D.H. Deng, X.Q. Chen, L. Yu, X. Wu, Q.F. Liu, Y.X. Liu, H. Yang, H.F. Tian, Y.F. Hu, P.P. Du, R. Si, J.H. Wang, X.J. Cui, H.B. Li, J.P. Xiao, T. Xu, J. Deng, F. Yang, P.N. Duchesne, P. Zhang, J.G. Zhou, L.T. Sun, J.Q. Li, X.L. Pan, X.H. Bao, A single iron site confined in a graphene matrix for the catalytic oxidation of benzene at room temperature, *Sci. Adv.* 1 (2015) e1500462.
- [5] M. Li, S.J. Wu, X.Y. Yang, J. Hu, L. Peng, L. Bai, Q.S. Huo, J.Q. Guan, Highly efficient single atom cobalt catalyst for selective oxidation of alcohols, *Appl. Catal. A* 543 (2017) 61-66.
- [6] W.G. Liu, L.L. Zhang, X. Liu, X.Y. Liu, X.F. Yang, S. Miao, W.T. Wang, A.Q. Wang, T. Zhang, Discriminating Catalytically Active FeN<sub>x</sub> Species of Atomically Dispersed Fe-N-C Catalyst for Selective Oxidation of the C-H Bond, *J. Am. Chem. Soc.* 139 (2017) 10790-10798.

- [7] L.L. Zhang, A.Q. Wang, W.T. Wang, Y.Q. Huang, X.Y. Liu, S. Miao, J.Y. Liu, T. Zhang, Co–N–C catalyst for C–C coupling reactions: on the catalytic performance and active sites, *ACS Catal.* 5 (2015) 6563-6572.
- [8] J.H. Xie, K.H. Yin, A. Serov, K. Artyushkova, H.N. Pham, X.H. Sang, R.R. Unocic, P. Atanassov, A.K. Datye, R.J. Davis, Selective aerobic oxidation of alcohols over atomically-dispersed non-precious metal catalysts, *ChemSusChem* 10 (2017) 359-362.
- [9] G. Wu, K.L. More, C.M. Johnston, P. Zelenay, High-performance electrocatalysts for oxygen reduction derived from polyaniline, iron, and cobalt, *Science* 332 (2011) 443-447.
- [10] K. Artyushkova, A. Serov, S. Rojas-Carbonell, P. Atanassov, Chemistry of multitudinous active sites for oxygen reduction reaction in transition metal–nitrogen–carbon electrocatalysts, *J. Phys. Chem. C* 119 (2015) 25917-25928.
- [11] C.H. Choi, W.S. Choi, O. Kasian, A.K. Mechler, M.T. Sougrati, S. Bruller, K. Strickland, Q. Jia, S. Mukerjee, K.J.J. Mayrhofer, F. Jaouen, Unraveling the nature of sites active toward hydrogen peroxide reduction in Fe-N-C catalysts, *Angew. Chem., Int. Ed.* 56 (2017) 1-5.
- [12] E. Proietti, F. Jaouen, M. Lefevre, N. Larouche, J. Tian, J. Herranz, J.P. Dodelet, Iron-based cathode catalyst with enhanced power density in polymer electrolyte membrane fuel cells, *Nat. Commun.* 2 (2011) 1-9.
- [13] J. Liu, X.J. Sun, P. Song, Y.W. Zhang, W. Xing, W.L. Xu, High-performance oxygen reduction electrocatalysts based on cheap carbon black, nitrogen, and trace iron, *Adv. Mater.* 25 (2013) 6879-6883.

- [14] M. Hasan, M. Musawir, P.N. Davey, I.V. Kozhevnikov, Oxidation of primary alcohols to aldehydes with oxygen catalysed by tetra-n-propylammonium perruthenate, *J. Mol. Catal. A: Chem.* 180 (2002) 77-84.
- [15] S. Mori, M. Takubo, K. Makida, T. Yanase, S. Aoyagi, T. Maegawa, Y. Monguchi, H. Sajiki, A simple and efficient oxidation of alcohols with ruthenium on carbon, *Chem. Commun.* (2009) 5159-5161.
- [16] W. Adam, F.G. Gelalcha, C.R. Saha-Moller, V.R. Stegmann, Chemoselective C-H oxidation of alcohols to carbonyl compounds with iodosobenzene catalyzed by (salen)chromium complex, *J. Org. Chem.* 65 (2000) 1915-1918.
- [17] T. Nishimura, T. Onoue, K. Ohe, S. Uemura, Palladium(II)-catalyzed oxidation of alcohols to aldehydes and ketones by molecular oxygen, *J. Org. Chem.* 64 (1999) 6750-6755.
- [18] G.T. Whiting, S.A. Kondrat, C. Hammond, N. Dimitratos, Q. He, D.J. Morgan, N.F. Dummer, J.K. Bartley, C.J. Kiely, S.H. Taylor, G.J. Hutchings, Methyl formate formation from methanol oxidation using supported gold-palladium nanoparticles, *ACS Catal.* 5 (2015) 637-644.
- [19] H. Wang, W. Fan, Y. He, J. Wang, J.N. Kondo, T. Tatsumi, Selective oxidation of alcohols to aldehydes/ketones over copper oxide-supported gold catalysts, *J. Catal.* 299 (2013) 10-19.
- [20] P.Y. Qi, S.S. Chen, J. Chen, J.W. Zheng, X.L. Zheng, Y.Z. Yuan, Catalysis and reactivation of ordered mesoporous carbon-supported gold nanoparticles for the base-free oxidation of glucose to gluconic acid, *ACS Catal.* 5 (2015) 2659-2670.
- [21] V.V. Costa, M. Estrada, Y. Demidova, I. Prosvirin, V. Kriventsov, R.F. Cotta, S. Fuentes, A. Simakov, E.V. Gusevskaya, Gold nanoparticles supported on magnesium oxide as

- catalysts for the aerobic oxidation of alcohols under alkali-free conditions, *J. Catal.* 292 (2012) 148-156.
- [22] A. Li, P. Zhang, X.X. Chang, W.T. Cai, T. Wang, J.L. Gong, Gold nanorod@TiO<sub>2</sub> yolk-shell nanostructures for visible-light-driven photocatalytic oxidation of benzyl alcohol, *Small* 11 (2015) 1892-1899.
- [23] J. Nie, J. Xie, H. Liu, Efficient aerobic oxidation of 5-hydroxymethylfurfural to 2,5-diformylfuran on supported Ru catalysts, *J. Catal.* 301 (2013) 83-91.
- [24] S.S. Chen, P.Y. Qi, J. Chen, Y.Z. Yuan, Platinum nanoparticles supported on N-doped carbon nanotubes for the selective oxidation of glycerol to glyceric acid in a base-free aqueous solution, *RSC Adv.* 5 (2015) 31566-31574.
- [25] C.M. Zhou, W.P. Deng, X.Y. Wan, Q.H. Zhang, Y.H. Yang, Y. Wang, Functionalized carbon nanotubes for biomass conversion: the base-free aerobic oxidation of 5-hydroxymethylfurfural to 2,5-furandicarboxylic acid over platinum supported on a carbon nanotube catalyst, *ChemCatChem* 7 (2015) 2853-2863.
- [26] J. Artz, S. Mallmann, R. Palkovits, Selective aerobic oxidation of HMF to 2,5-diformylfuran on covalent triazine frameworks-supported Ru catalysts, *ChemSusChem* 8 (2015) 672-679.
- [27] A. Takagaki, M. Takahashi, S. Nishimura, K. Ebitani, One-pot synthesis of 2,5-diformylfuran from carbohydrate derivatives by sulfonated resin and hydrotalcite-supported ruthenium catalysts, *ACS Catal.* 1 (2011) 1562-1565.
- [28] R.Q. Fang, R. Luque, Y.W. Li, Selective aerobic oxidation of biomass-derived HMF to 2,5-diformylfuran using a MOF-derived magnetic hollow Fe-Co nanocatalyst, *Green Chem.* 18 (2016) 3152-3157.

- [29] B. Liu, Z.H. Zhang, K. Lv, K.J. Deng, H.M. Duan, Efficient aerobic oxidation of biomass-derived 5-hydroxymethylfurfural to 2,5-diformylfuran catalyzed by magnetic nanoparticle supported manganese oxide, *Appl. Catal. A* 472 (2014) 64-71.
- [30] J.F. Nie, H.C. Liu, Efficient aerobic oxidation of 5-hydroxymethylfurfural to 2,5-diformylfuran on manganese oxide catalysts, *J. Catal.* 316 (2014) 57-66.
- [31] H. Watanabe, S. Asano, S. Fujita, H. Yoshida, M. Arai, Nitrogen-doped, metal-free activated carbon catalysts for aerobic oxidation of alcohols, *ACS Catal.* 5 (2015) 2886-2894.
- [32] I. Sádaba, Y.Y. Gorbanev, S. Kegnaes, S.S.R. Putluru, R.W. Berg, A. Riisager, Catalytic performance of zeolite-supported vanadia in the aerobic oxidation of 5-hydroxymethylfurfural to 2,5-diformylfuran, *ChemCatChem* 5 (2013) 284-293.
- [33] N.T. Le, P. Lakshmanan, K. Cho, Y. Han, H. Kim, Selective oxidation of 5-hydroxymethyl-2-furfural into 2,5-diformylfuran over  $\text{VO}^{2+}$  and  $\text{Cu}^{2+}$  ions immobilized on sulfonated carbon catalysts, *Appl. Catal. A* 464-465 (2013) 305-312.
- [34] F. Neatu, R.S. Marin, M. Florea, N. Petrea, O.D. Pavel, V.I. Pârvulescu, Selective oxidation of 5-hydroxymethyl furfural over non-precious metal heterogeneous catalysts, *Appl. Catal. B* 180 (2016) 751-757.
- [35] L.N. Kong, W. Wei, Q.F. Zhao, J.Q. Wang, Y. Wan, Active coordinatively unsaturated manganese monoxide-containing mesoporous carbon catalyst in wet peroxide oxidation, *ACS Catal.* 2 (2012) 2577-2586.
- [36] T. Wang, Y.L. Meng, L.A. Zeng, J.L. Gong, Selective oxidation of methanol to dimethoxymethane over  $\text{V}_2\text{O}_5/\text{TiO}_2\text{-Al}_2\text{O}_3$  catalysts, *Sci. Bull.* 60 (2015) 1009-1018.

- [37] Z.F. Yuan, W.N. Zhao, Z.P. Liu, B.Q. Xu, NaOH alone can be a homogeneous catalyst for selective aerobic oxidation of alcohols in water, *J. Catal.* 353 (2017) 37-43.
- [38] Y. Iwasawa, *X-ray absorption fine structure for catalysts and surfaces*, World Scientific, Singapore, 1966.
- [39] T. Taguchi, REX2000 Version 2.5: Improved DATA Handling and Enhanced User-Interface, in: *AIP Conference Proceedings*, 2006.
- [40] T. Taguchi, T. Ozawa, H. Yashiro, REX2000: yet another XAFS analysis package, *Phys. Scripta T115* (2005) 205-206.
- [41] J.J. Rehr, R. Albers, Theoretical approaches to x-ray absorption fine structure, *Rev. Mod. Phys.* 72 (2000) 621-654.
- [42] A.L. Ankudinov, B. Ravel, J.J. Rehr, S.D. Conradson, Real space multiple scattering calculation of XANES, *Phys. Rev. B: Condens. Matter Mater. Phys.* 58 (1998) 7565-7565.
- [43] P.B. Weisz, C.D. Prater, Interpretation of measurements in experimental catalysis, *Adv. Catal.* 6 (1954) 143-196.
- [44] S.T. Oyama, X.M. Zhang, J.Q. Lu, Y.F. Gu, T. Fujitani, Epoxidation of propylene with H<sub>2</sub> and O<sub>2</sub> in the explosive regime in a packed-bed catalytic membrane reactor, *J. Catal.* 257 (2008) 1-4.
- [45] L.M. Malard, M.A. Pimenta, G. Dresselhaus, M.S. Dresselhaus, Raman spectroscopy in graphene, *Phys. Rep.* 473 (2009) 51-87.
- [46] M.A. Pimenta, G. Dresselhaus, M.S. Dresselhaus, L.G. Cancado, A. Jorio, R. Saito, Studying disorder in graphite-based systems by Raman spectroscopy, *Phys. Chem. Chem. Phys.* 9 (2007) 1276-1291.

- [47] X.D. Yang, Y. Zheng, J. Yang, W. Shi, J.H. Zhong, C. Zhang, X. Zhang, Y.H. Hong, X.X. Peng, Z.Y. Zhou, S.G. Sun, Modeling Fe/N/C Catalysts in Monolayer Graphene, *ACS Catal.* 7 (2016) 139-145.
- [48] T.Y. Cheng, H. Yu, F. Peng, H.J. Wang, B.S. Zhang, D.S. Su, Identifying active sites of CoNC/CNT from pyrolysis of molecularly defined complexes for oxidative esterification and hydrogenation reactions, *Catal. Sci. Technol.* 6 (2016) 1007-1015.
- [49] D.H. Guo, R. Shibuya, C. Akiba, S. Saji, T. Kondo, J. Nakamura, Active sites of nitrogen-doped carbon materials for oxygen reduction reaction clarified using model catalysts, *Science* 351 (2016) 361-365.
- [50] K. Artyushkova, B. Kiefer, B. Halevi, A. Knop-Gericke, R. Schlogl, P. Atanassov, Density functional theory calculations of XPS binding energy shift for nitrogen-containing graphene-like structures, *Chem. Commun.* 49 (2013) 2539-2541.
- [51] R.T. Lv, T.X. Cui, M.S. Jun, Q. Zhang, A.Y. Cao, D.S. Su, Z.J. Zhang, S.H. Yoon, J. Miyawaki, I. Mochida, F.Y. Kang, Open-ended, N-doped carbon nanotube-graphene hybrid nanostructures as high-performance catalyst support, *Adv. Funct. Mater.* 21 (2011) 999-1006.
- [52] H.L. Peng, Z.Y. Mo, S.J. Liao, H.G. Liang, L.J. Yang, F. Luo, H.Y. Song, Y.L. Zhong, B.Q. Zhang, High performance Fe- and N- doped carbon catalyst with graphene structure for oxygen reduction, *Sci. Rep.* 3 (2013) 1-7.
- [53] F. Gao, Y. Zheng, R.K. Kukkadapu, Y. Wang, E.D. Walter, B. Schwenzer, J. Szanyi, C.H.F. Peden, Iron loading effects in Fe/SSZ-13 NH<sub>3</sub>-SCR catalysts: nature of the Fe ions and structure–function relationships, *ACS Catal.* 6 (2016) 2939-2954.

- [54] A.V. Kucherov, M. Shelef, Quantitative determination of isolated  $\text{Fe}^{3+}$  cations in FeHZSM-5 catalysts by ESR, *J. Catal.* 195 (2000) 106-112.
- [55] M.S. Kumar, M. Schwidder, W. Grünert, A. Brückner, On the nature of different iron sites and their catalytic role in Fe-ZSM-5 DeNO<sub>x</sub> catalysts: new insights by a combined EPR and UV/VIS spectroscopic approach, *J. Catal.* 227 (2004) 384-397.
- [56] U.I. Kramm, I. Herrmann-Geppert, J. Behrends, K. Lips, S. Fiechter, P. Bogdanoff, On an easy way to prepare metal-nitrogen doped carbon with exclusive presence of  $\text{MeN}_4$ -type sites active for the ORR, *J. Am. Chem. Soc.* 138 (2016) 635-640.
- [57] A.N. Vasiliev, L.V. Shvanskaya, O.S. Volkova, A.V. Koshelev, E.A. Zvereva, G.V. Raganyan, I.A. Presniakov, A.V. Sobolev, A.M. Abakumov, Y.M. Lvov, Magnetism of natural composite of halloysite clay nanotubes  $\text{Al}_2\text{Si}_2\text{O}_5(\text{OH})_4$  and amorphous hematite  $\text{Fe}_2\text{O}_3$ , *Mater. Charact.* 129 (2017) 179-185.
- [58] S.R. Pelluri, R. Singh, ESR and magnetization studies of  $\text{Fe}_2\text{O}_3$ - $\text{Bi}_2\text{O}_3$ - $\text{ZnO}$ - $\text{PbO}$  glass system, *J. Magn. Magn. Mater* 418 (2016) 206-212.
- [59] I. Ardelean, G. Salvan, M. Peteanu, V. Simon, C. Himcinschi, F. Ciorcas, EPR and magnetic susceptibility studies of  $\text{B}_2\text{O}_3$ - $\text{SrO}$ - $\text{Fe}_2\text{O}_3$  glasses, *Mod. Phys. Lett. B* 13 (1999) 801-808.
- [60] N. Ramaswamy, U. Tylus, Q. Jia, S. Mukerjee, Activity descriptor identification for oxygen reduction on nonprecious electrocatalysts: linking surface science to coordination chemistry, *J. Am. Chem. Soc.* 135 (2013) 15443-15449.
- [61] X. Cui, Y. Li, S. Bachmann, M. Scalone, A.E. Surkus, K. Junge, C. Topf, M. Beller, Synthesis and characterization of iron-nitrogen-doped graphene/core-shell catalysts:

efficient oxidative dehydrogenation of N-heterocycles, *J. Am. Chem. Soc.* 137 (2015) 10652-10658.

- [62] V.V. Strelko, V.S. Kuts, P.A. Thrower, On the mechanism of possible influence of heteroatoms of nitrogen, boron and phosphorus in a carbon matrix on the catalytic activity of carbons in electron transfer reactions, *Carbon* 38 (2000) 1499-1503.

## Table and Figure captions

**Table 1** Elemental analyses of the FeN<sub>x</sub>/C-*T* catalysts obtained at different pyrolysis temperatures.

**Table 2** Conversion and product distribution for the oxidation of different alcohols over FeN<sub>x</sub>/C-900 catalyst.

**Scheme 1.** The proposed catalytic pathway for the selective oxidation of HMF over FeN<sub>x</sub>/C-*T* catalysts.

**Fig. 1.** TEM and HAADF-STEM images of FeN<sub>x</sub>/C-900. (a) bright-field image, (b) and (c) dark-field images, and (d) STEM mapping image.

**Fig. 2.** HMF conversion and DFF selectivity on the FeN<sub>x</sub>/C-*T* catalysts by different pyrolysis temperatures. Reaction conditions: HMF (0.25 mmol, 32 mg), FeN<sub>x</sub>/C-*T* (0.1 g), DMF (10 mL), 100 °C, 1 h, and O<sub>2</sub> (0.5 MPa).

**Fig. 3.** The TOF value of HMF oxidation on the FeN<sub>x</sub>/C-*T* catalysts by different pyrolysis temperatures.

**Fig. 4.** HMF conversion and DFF selectivity on the FeN<sub>x</sub>/C-900 catalyst as a function of reaction time. Reaction conditions: HMF (0.25 mmol, 32 mg), FeN<sub>x</sub>/C-900 (0.1 g), DMF (10 mL), 100 °C, and O<sub>2</sub> (0.5 MPa).

**Fig. 5.** N 1s XPS profiles of the FeN<sub>x</sub>/C-*T* catalysts. (a) FeN<sub>x</sub>/C-900, (b) FeN<sub>x</sub>/C-800, (c) FeN<sub>x</sub>/C-1000, (d) FeN<sub>x</sub>/C-700, and (e) FeN<sub>x</sub>/C-600.

**Fig. 6.** HMF conversion on the FeN<sub>x</sub>C/N-*T* catalysts with approximately equal N content. Reaction conditions: HMF (0.25 mmol, 32 mg), catalyst (0.1 g), DMF (10 mL), 100 °C, 1 h, and O<sub>2</sub> (0.5 MPa).

**Fig. 7.** ESR spectra of the FeN<sub>x</sub>/C-*T* catalysts with identical magnification and the same weight. (a) FeN<sub>x</sub>/C-1000, (b) FeN<sub>x</sub>/C-900, (c) FeN<sub>x</sub>/C-800, (d) FeN<sub>x</sub>/C-700, and (e) FeN<sub>x</sub>/C-600 at -173 °C.

**Fig. 8.** (A) The normalized XAFS profiles and (B) the  $k^3$ -weighted Fourier transform EXAFS profiles at Fe K-edge of different samples. (a) FeN<sub>x</sub>/C-900, (b) FeN<sub>x</sub>/C-800, (c) FeN<sub>x</sub>/C-700, (d) FeN<sub>x</sub>/C-600, (e) Fe<sub>2</sub>O<sub>3</sub>, and (f) Fe foil.

**Fig. 9.** The recycling result of FeN<sub>x</sub>/C-900 catalyst for the HMF oxidation. Reaction conditions: HMF (0.25 mmol, 32 mg), FeN<sub>x</sub>/C-900 (0.1 g), DMF (10 mL), 100 °C, 5 h, and O<sub>2</sub> (0.5 MPa). (a) The FeN<sub>x</sub>/C-900 catalyst was reused after calcination in N<sub>2</sub> at 900 °C for 1 h and (b) the FeN<sub>x</sub>/C-900 catalyst after the 3rd run was calcined in 3%NH<sub>3</sub>/N<sub>2</sub> for 1 h at 900 °C and then reused.

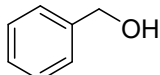
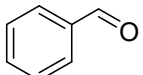
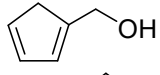
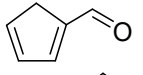
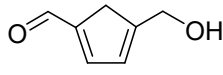
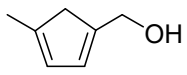
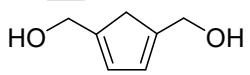
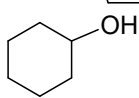
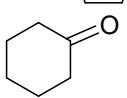
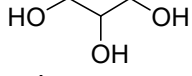
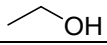
**Table 1**Elemental analyses of the FeN<sub>x</sub>/C-*T* catalysts obtained at different pyrolysis temperatures.

Catalyst	C/N	Content / wt. %			
		N <sup>a</sup>	C <sup>a</sup>	H <sup>a</sup>	Fe <sup>b</sup>
FeN <sub>x</sub> /C-1000	34.0	2.7	91.8	0.9	1.31
FeN <sub>x</sub> /C-900	20.3	4.3	87.3	1.7	0.90
FeN <sub>x</sub> /C-800	11.1	7.4	82.5	1.6	1.10
FeN <sub>x</sub> /C-700	7.2	10.7	77.1	1.9	1.38
FeN <sub>x</sub> /C-600	5.5	14.4	78.9	2.2	0.89

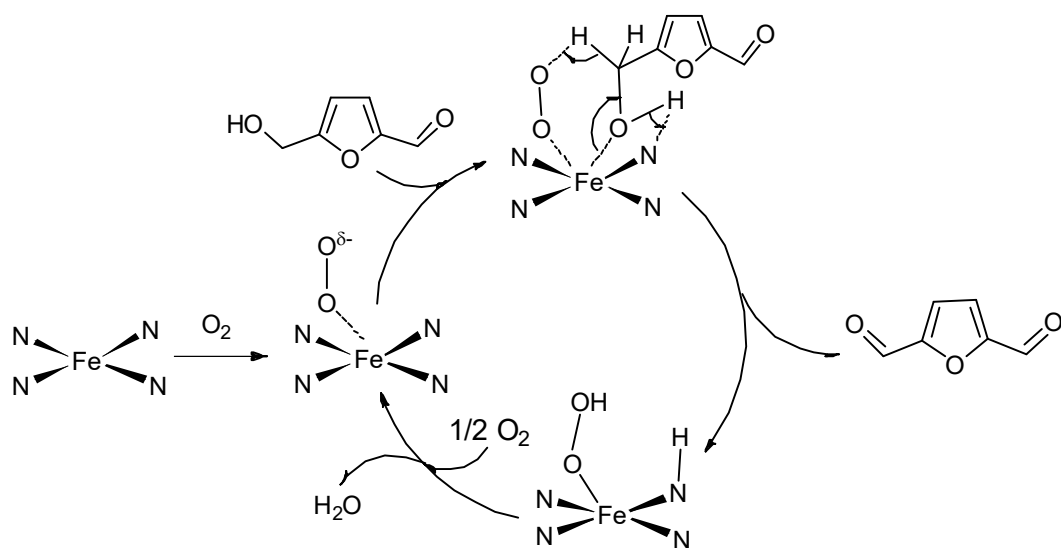
a: analyzed by element analysis; b: measured by XRF.

**Table 2**

Conversion and product distribution for the oxidation of different alcohols over FeN<sub>x</sub>/C-900 catalyst.

Entry	Substrate	Product	Conv. / mol %	Selec. / mol %
1			100	98.6
2			100	100
3			99.5	97.3
4			63.9	100
5			99.3	81.5
6			16.6	38.8
7		—	0	0
8		—	0	0

Reaction conditions: substrate (0.25 mmol, except of 2,5-furandimethanol for 0.125 mmol ) and FeN<sub>x</sub>/C-900 catalyst (0.1 g), DMF (10 mL), 100 °C (except of benzyl alcohol at 80 °C) , 10 h, O<sub>2</sub> (0.5 MPa).



**Scheme 1.** The proposed catalytic pathway for the selective oxidation of HMF over  $FeN_x/C-T$  catalysts.

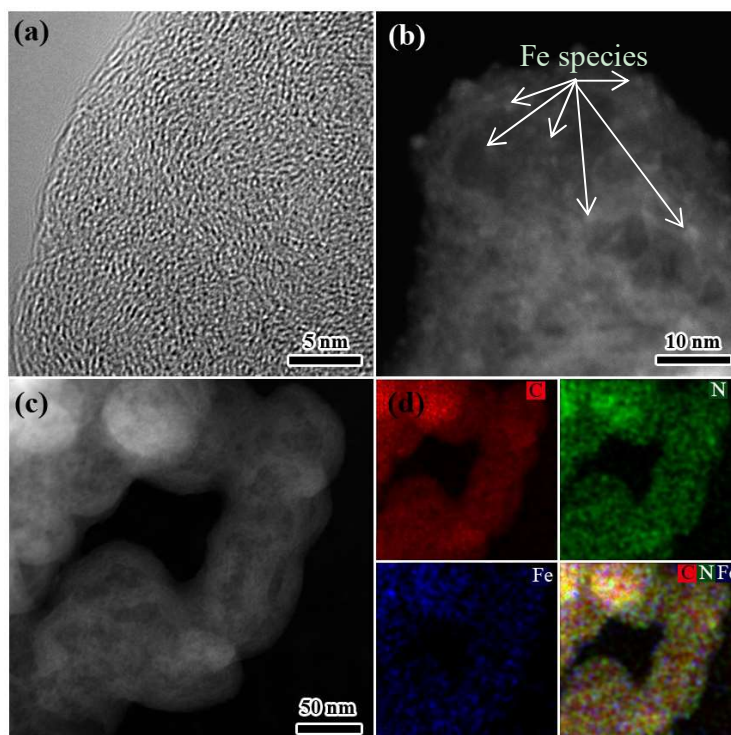


**Fig. 1.** TEM and HAADF-STEM images of FeN<sub>x</sub>/C-900. (a) bright-field image, (b) and (c) dark-field images, and (d) STEM mapping image.

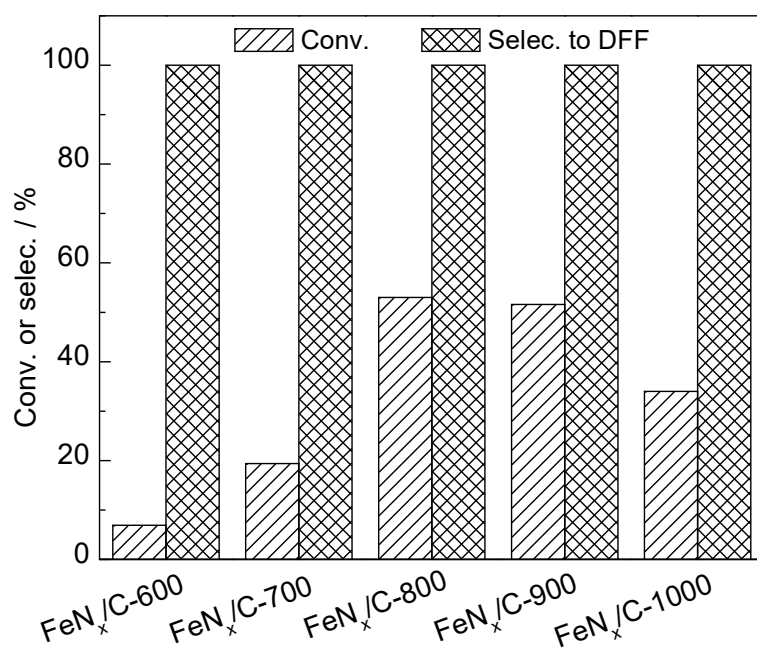


**Fig. 2.** HMF conversion and DFF selectivity on the FeN<sub>x</sub>/C-*T* catalysts by different pyrolysis temperatures. Reaction conditions: HMF (0.25 mmol, 32 mg), FeN<sub>x</sub>/C-*T* (0.1 g), DMF (10 mL), 100 °C, 1 h, and O<sub>2</sub> (0.5 MPa).

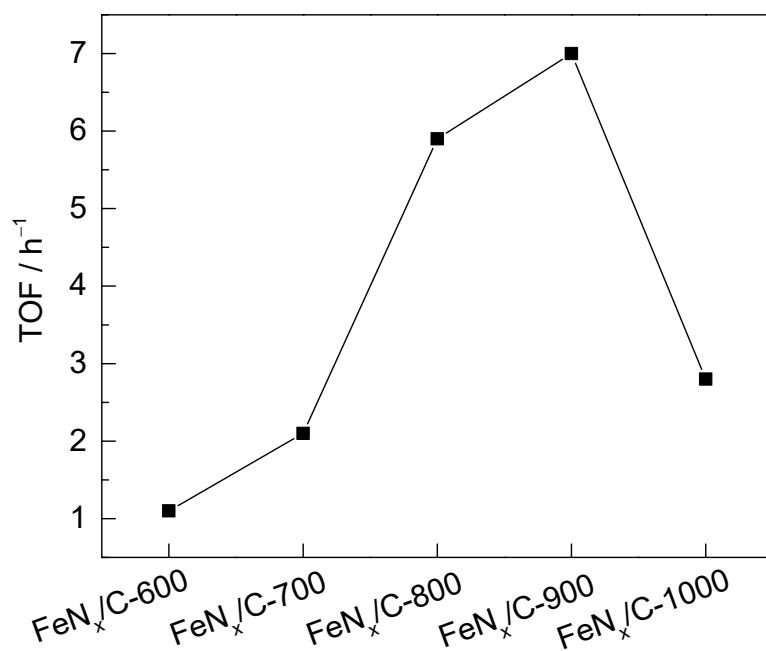


**Fig. 3.** The TOF value of HMF oxidation on the FeN<sub>x</sub>/C-*T* catalysts by different pyrolysis temperatures.

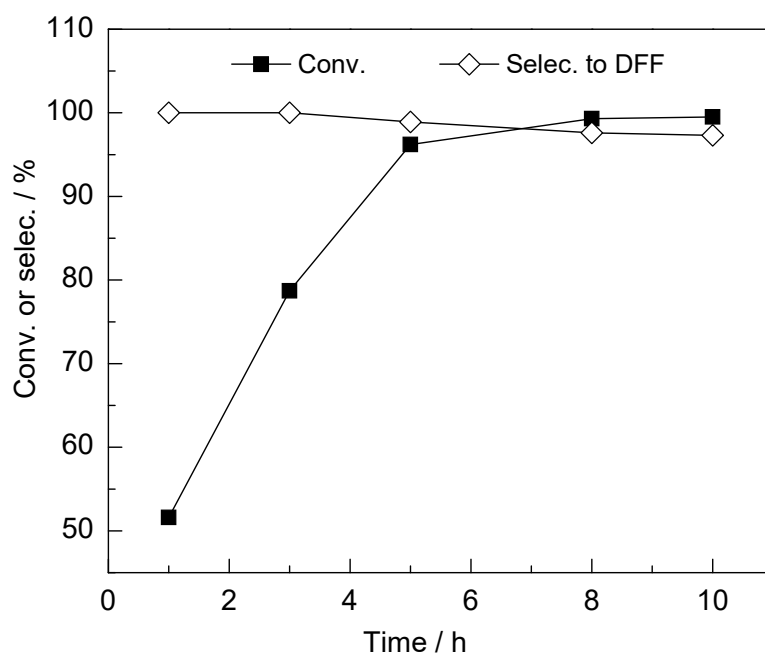


**Fig. 4.** HMF conversion and DFF selectivity on the FeN<sub>x</sub>/C-900 catalyst as a function of reaction time. Reaction conditions: HMF (0.25 mmol, 32 mg), (0.1 g), DMF (10 mL), 100 °C, and O<sub>2</sub> (0.5 MPa).

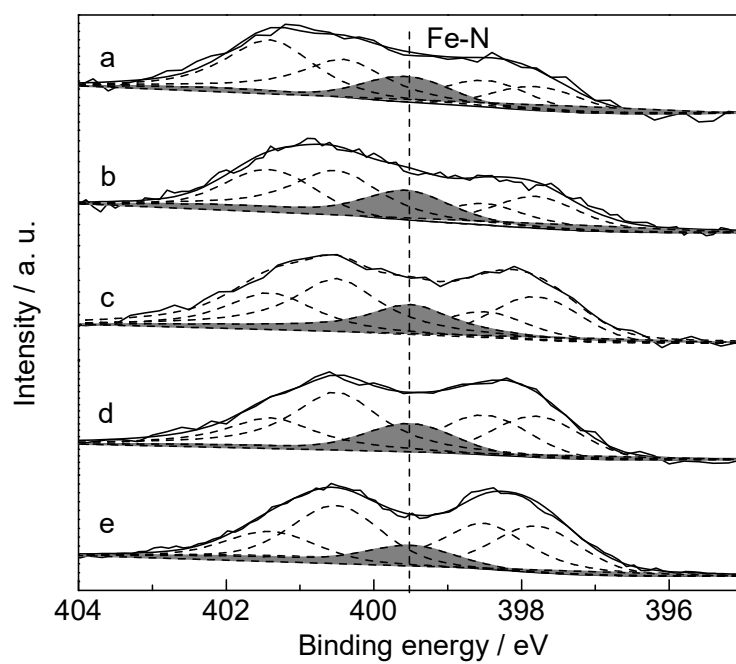


**Fig. 5.** N 1s XPS profiles of the FeN<sub>x</sub>/C-*T* catalysts. (a) FeN<sub>x</sub>/C-900, (b) FeN<sub>x</sub>/C-800, (c) FeN<sub>x</sub>/C-1000, (d) FeN<sub>x</sub>/C-700, and (e) FeN<sub>x</sub>/C-600.

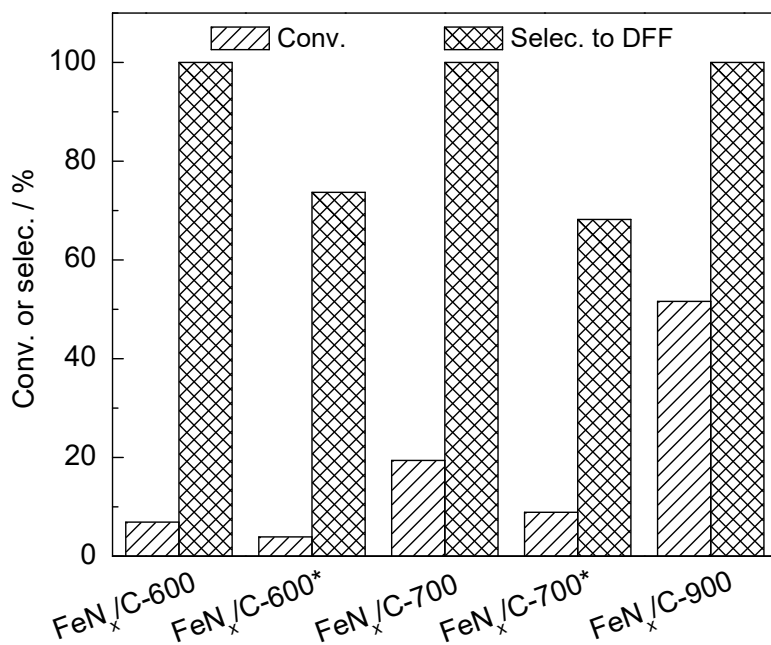


**Fig. 6.** HMF conversion on the FeN<sub>x</sub>C/N-*T* catalysts with approximately equal N content.

Reaction conditions: HMF (0.25 mmol, 32 mg), catalyst (0.1 g), DMF (10 mL), 100 °C, 1 h, and O<sub>2</sub> (0.5 MPa).

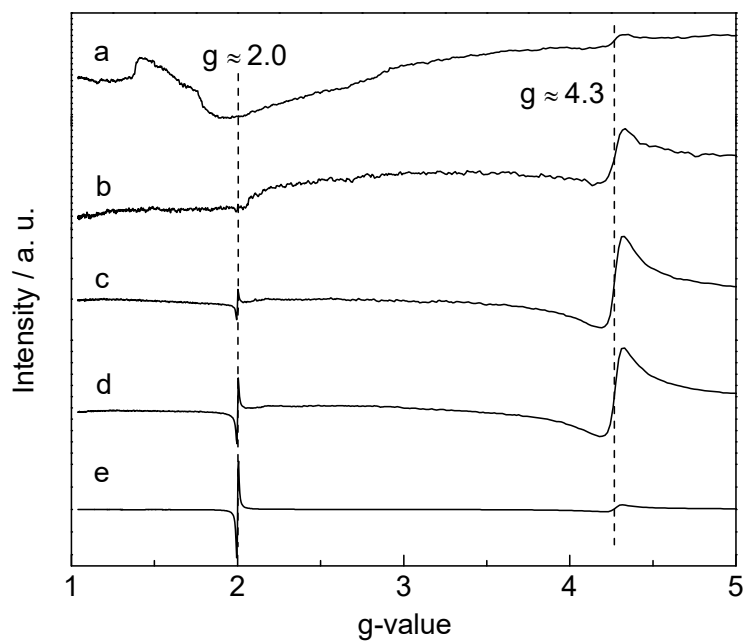


**Fig. 7.** ESR spectra of the FeN<sub>x</sub>/C-*T* catalysts with identical magnification and the same weight. (a) FeN<sub>x</sub>/C-1000, (b) FeN<sub>x</sub>/C-900, (c) FeN<sub>x</sub>/C-800, (d) FeN<sub>x</sub>/C-700, and (e) FeN<sub>x</sub>/C-600 at -173 °C.

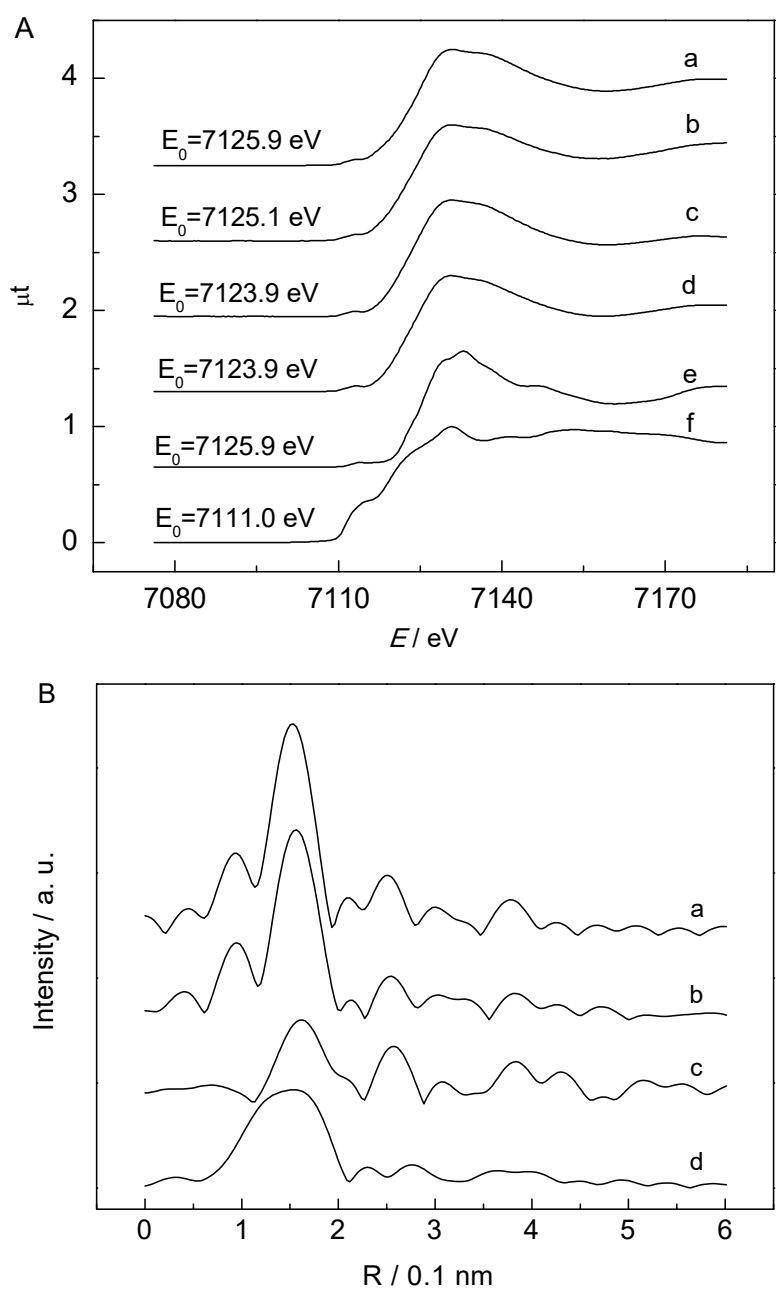


**Fig. 8.** (A) The normalized XAFS profiles and (B) the  $k^3$ -weighted Fourier transform EXAFS profiles at Fe K-edge of different samples. (a) FeN<sub>x</sub>/C-900, (b) FeN<sub>x</sub>/C-800, (c) FeN<sub>x</sub>/C-700, (d) FeN<sub>x</sub>/C-600, (e) Fe<sub>2</sub>O<sub>3</sub>, and (f) Fe foil.

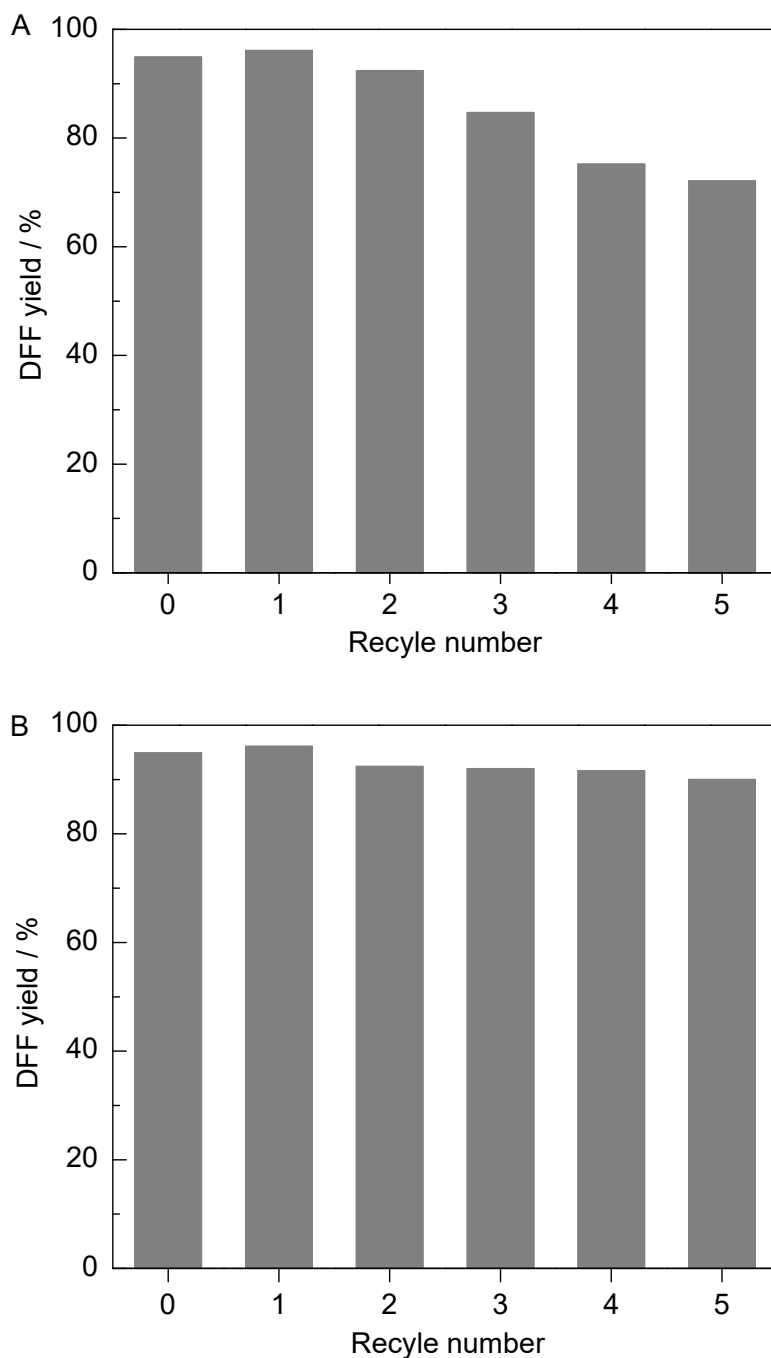


**Fig. 9.** Recycling results of the FeN<sub>x</sub>/C-900 catalyst for the HMF oxidation. Reaction conditions: HMF (0.25 mmol, 32 mg), FeN<sub>x</sub>/C-900 (0.1 g), DMF (10 mL), 100 °C, 5 h, and O<sub>2</sub> (0.5 MPa). (A) The FeN<sub>x</sub>/C-900 catalyst was reused after calcination in N<sub>2</sub> at 900 °C for 1 h and (B) the FeN<sub>x</sub>/C-900 catalyst after the 3rd run was calcined in 3%NH<sub>3</sub>/N<sub>2</sub> for 1 h at 900 °C and

then reused.